EES Catalysis

PAPER

View Article Online
View Journal

Open Access Article. Published on 04 February 2026. Downloaded on 4/28/2026 3:51:50 AM.
This article is licensed under a Creative Commons Attribution-NonCommercial 3.0 Unported Licence.

Cite this: DOI: 10.1039/d5ey00299k

Tailoring electronic structures of Ni@N-doped carbon hollow urchins for dual-functional Zn–CO_2 batteries and industrial CO_2 electroreduction

Songjiang Wu,†[ac] Di Wang,†[b] Haijian Wang,[c] Haiyan Chen,[c] Xinyu Zhuang,[b] Shenjie Yu,[c] Hao Zhang, *[d] Suqin Ci *[a] and Zhenhai Wen *[bc]

Received 17th October 2025,
Accepted 22nd December 2025

DOI: 10.1039/d5ey00299k

rsc.li/eescatalysis

A catalyst with a hollow urchin-like sphere structure and porous surface was synthesized using Ni-MOF precursors (Ni@N-HCS). This catalyst features nickel nanoparticles encapsulated by nitrogen-doped carbon shells and exhibits excellent electrocatalytic activity in the CO_2 reduction reaction (CO_2RR). In a hybrid flow cell, the optimal catalyst attains an industrial current density of 174.23 mA cm^{-2} and a high CO Faraday efficiency (FE_{CO}) of 82.34%, along with good long-term stability. Moreover, when employed as the cathode in a Zn–CO_2 flow battery, this catalyst achieves the highest power density of 11.55 mW cm^{-2} and demonstrates excellent cycling durability. According to density functional theory (DFT) calculations, the graphene-covered Ni cluster (Ni-ApyN) is identified as the most efficient active site for the CO_2RR. This efficiency is attributed to the fact that pyridinic N-doped carbon shell encapsulating Ni nanoparticles (NPs) reduces the free energy of the reaction by modulating the electronic structure of Ni, thereby effectively accelerating the reaction kinetics rate. As a result, this work in both the hybrid flow cell and the Zn–CO_2 flow battery offers a promising approach for energy storage and conversion.

Broader context

Based on nickel metal–organic framework precursors, this work develops a hollow urchin-like spherical catalyst composed of nitrogen-doped carbon shells encapsulating Ni nanoparticles (Ni@N-HCS). The material demonstrates outstanding electrocatalytic performance for CO_2 reduction reaction (CO_2RR), achieving an industrial-level current density of 174.23 mA cm^{-2} and a high CO Faraday efficiency of 82.34% in a hybrid flow cell, along with remarkable stability. When applied in a Zn–CO_2 flow battery, it enables a peak power density of 11.55 mW cm^{-2} and superior cycling durability. This study offers an effective catalyst design strategy and a promising route for advancing energy conversion and storage technologies toward a carbon-neutral future.

Introduction

Electrochemical CO_2 reduction has emerged as a promising strategy to address environmental and energy challenges, providing solutions for surplus power storage and the value-added conversion of CO_2.[1] However, this process faces significant challenges due to the inherent stability of CO_2 molecules and the simultaneous presence of the competing hydrogen evolution reaction (HER) in aqueous electrolytes.[2,3] Therefore, it is imperative to develop efficient electrocatalysts capable of achieving high current densities and demonstrating superior selectivity towards CO_2 reduction reaction (CO_2RR) products. Structural optimization is crucial for improving the catalytic performance of electrocatalysts. Recently, there has been a significant interest in utilizing hollow and porous structural materials for CO_2 reduction reactions due to their

---

[a] Fujian Provincial Key Laboratory of Soil Environmental Health and Regulation, College of Resources and Environment, Fujian Agriculture and Forestry University, Fuzhou 350002, China. E-mail: sqci@fafu.edu.cn

[b] CAS Key Laboratory of Design and Assembly of Functional Nanostructures, and Fujian Provincial Key Laboratory of Materials and Techniques toward Hydrogen Energy, Fujian Institute of Research on the Structure of Matter, Chinese Academy of Sciences, Fuzhou, Fujian, 350002, China. E-mail: wen@fjirsm.ac.cn

[c] Key Laboratory of Jiangxi Province for Persistent Pollutants Control, National-Local Joint Engineering Research Center of Heavy Metals Pollutants Control and Resource Utilization and Resources Recycle, Nanchang Hangkong University, Nanchang, Jiangxi, 330063, China

[d] Department of Chemical Engineering, Massachusetts Institute of Technology, Cambridge, MA 02139, USA. E-mail: hzhchem@mit.edu

† These authors contributed equally to this work.

© 2026 The Author(s). Published by the Royal Society of Chemistry

Open Access Article. Published on 04 February 2026. Downloaded on 4/28/2026 3:51:50 AM.
This article is licensed under a Creative Commons Attribution-NonCommercial 3.0 Unported Licence.

advantageous properties, including improved electron transport, high electrical conductivity, and large specific surface area.[4–7] However, traditional methods for synthesizing hollow structural materials, such as employing soft, hard, or sacrificial templates, face limitations because of their complexity, time consumption, and associated drawbacks.[8–10]

Recent studies have demonstrated that metal–organic frameworks (MOFs) can serve as efficient self-templates for the synthesis of hollow/porous structures.[11–13] Under inert conditions, thermal treatment induces the carbonization reactions of the organic ligands in hollow MOFs, leading to the formation of materials with porous/hollow structures inherent to the MOF precursors themselves.[14,15] As a result, catalyst materials derived from MOFs exhibit exceptional electrochemical performance, making them highly promising candidates for efficient and selective CO_2RR. Research on flow cells holds significant implications for the industrialization of CO_2RR, as evidenced by notable advancements in gas diffusion electrodes and flow cell devices that have achieved remarkable success in attaining industrial-scale current densities.[16,17] Additionally, Zn–CO_2 batteries offer a unique combination of CO_2 utilization and energy output, with notable benefits such as high theoretical energy densities, abundant raw materials and high safety levels.[18–20] The utilization of Zn–CO_2 batteries provides a novel and sustainable approach to effectively address pressing environmental and energy challenges by simultaneously tackling CO_2 emissions and meeting the growing energy demands.

Here, a nitrogen-doped surface porous hollow urchin-like carbon sphere-encapsulated nickel nanoparticle material (Ni@N-HCS) was successfully synthesized through the pyrolysis of hollow-structured MOF precursors. Ni@N-HCS-800 exhibited remarkable electrochemical CO_2 reduction performance in the flow cell, maintaining an impressive faradaic efficiency of 82.34% for CO production and achieving a high CO partial current density of 174.23 mA cm^{-2}, while displaying excellent long-term stability. Moreover, gas diffusion electrodes were employed to improve the mass transfer efficiency of CO_2 in the electrolyte of the Zn–CO_2 battery. The resulting Zn–CO_2 flow battery demonstrated exceptional stability during both charge and discharge cycles, achieving a maximum power density of 11.55 mW cm^{-2}. The experimental results, in conjunction with density functional theory (DFT) calculations, confirmed that the pyridine N-doped carbon layer coated with Ni NPs played a pivotal role in reducing the reaction energy barriers. This resulted in a highly active CO_2RR catalyst that exhibited impressive CO selectivity over a wide potential range.

Results and discussion

Synthesis and characterization

Fig. 1a illustrates the synthesis process of Ni@N-HCS-800. Initially, Ni-MOF was prepared and then coated with a DCDA protective shell. The material was subjected to controlled thermal annealing in an Ar atmosphere, where the DCDA shell served the dual function of safeguarding and stabilizing the hollow spherical structure of Ni-MOF. Simultaneously, the thermal decomposition of DCDA can generate carbon nitride and release reactive species such as $C_2N_2^+$, $C_3N_2^+$, and $C_3N_3^+$. These reactive species effectively facilitated the reduction of Ni-MOF to its metallic state.[21] Fig. S1 shows the hollow Ni-MOF precursor and the unetched Ni@N-HCS of urchin-like spheres with a rough surface. The resulting powder was then stirred in 1 M HCl for 12 h to generate abundant pores and defects while yielding a smoother surface.

SEM images, as depicted in Fig. 1b and Fig. S2, demonstrate that both Ni@N-HCS-700 and Ni@N-HCS-800 exhibited a distinctive morphology characterized by hollow urchin-like spheres with tentacles. On the contrary, the surface of Ni@N-HCS-900 appears to melt due to the increase in pyrolysis temperature, resulting in the formation of nanosheet-like structures. The presence of pores observed on the surface of Ni@N-HCS-800 can be attributed to the etching of metal particles using hydrochloric acid. To further illustrate the specific contribution of N-doping and urchin-like morphology, Ni@C-800 and Ni@HCS-800 catalysts are also prepared by a similar synthesized method. Ni@C-800 catalyst exhibits a similar hollow structure and Ni@HCS-800 presents an irregular morphology (Fig. S3). Consequently, N-doping plays a critical role in forming the urchin-like morphology, while the surfactant PVP controls the growth of spherical particles and prevents their aggregation.

Transmission electron microscopic (TEM) images depicted in Fig. 1c and d provide additional evidence of the hollow structure of Ni@N-HCS-800 and reveal the encapsulation of Ni nanoparticles (NPs) within a nitrogen-doped hollow carbon shell. HRTEM images (Fig. 1e and f) reveal the presence of the (002) plane of graphitic carbon with an interplanar spacing of approximately 0.33 nm. Additionally, clear lattice fringes with a spacing of 0.178 nm are observed, corresponding to the (200) plane of metallic nickel. The carbon layer coating around the Ni NPs allows reactants to access the Ni core while preventing Ni NPs from oxidation and aggregation in the presence of air. These properties are crucial for the catalysts to maintain a high level of electrocatalytic activity and long-term stability.[22] High-angle annular dark-field scanning transmission electron microscopy (HAADF-STEM) combined with energy-dispersive X-ray spectroscopy (EDS) elemental mapping images of Ni@N-HCS-800 (Fig. 1g) offered convincing evidence for the coexistence and dispersion of Ni, C, and N atoms. It is worth noting that the close correlation observed between the N and C signals in the mapping images indicated that the N element is uniformly distributed in the hollow carbon spheres.

Fig. 2a illustrates the X-ray powder diffraction (XRD) pattern of Ni@N-HCS. The detected peaks at 44.51°, 51.85°, and 76.37° correspond to the (111), (200), and (220) planes of Ni monomers, respectively (JPCDS no. 04-0850).[23] This indicates that the Ni ions present in Ni-MOFs are transformed into metallic Ni NPs after the pyrolysis process. Additionally, the peak observed at 26.3° corresponds to the (002) plane of graphitic carbon. The Raman spectra in Fig. 2b show characteristic peaks at approximately 1350 cm^{-1} (D band) and 1600 cm^{-1} (G band). The

© 2026 The Author(s). Published by the Royal Society of Chemistry

Open Access Article. Published on 04 February 2026. Downloaded on 4/28/2026 3:51:50 AM.
This article is licensed under a Creative Commons Attribution-NonCommercial 3.0 Unported Licence.

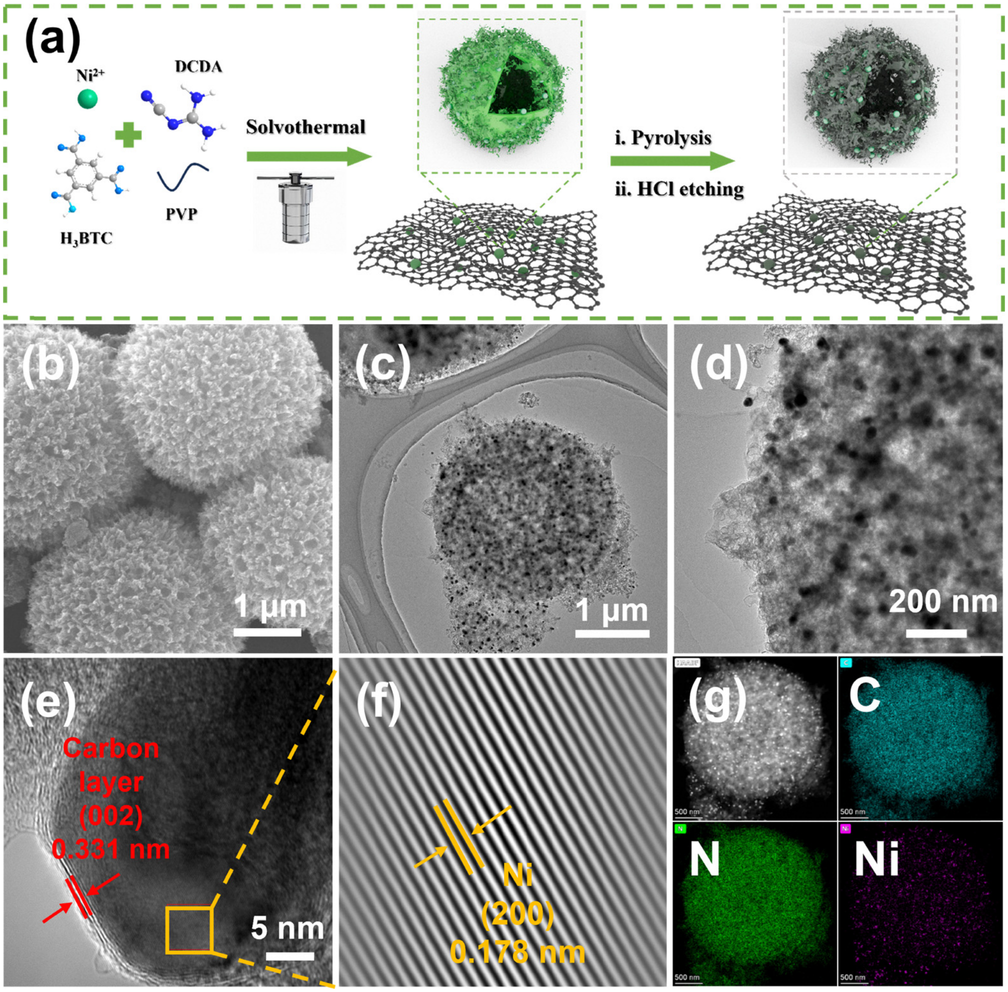

Fig. 1 Structural characterization of the Ni@N-HCS-800 catalyst. (a) Synthesis process diagram for the electrode material; (b) SEM image showing Ni@N-HCS-800; (c) and (d) TEM images of Ni@N-HCS-800; (e) and (f) HRTEM image and its magnified view for Ni@N-HCS-800; (g) HAADF-STEM image and corresponding EDS elemental mapping images of Ni@N-HCS-800.

intensity ratio of the D band to G band for Ni@N-HCS-800 is 1.27, which is higher than that of Ni@N-HCS-700 (1.19) and Ni@N-HCS-900 (1.25), suggesting the much more defects, a lower level of graphitization and the diminished structure order in Ni@N-HCS-800.[24]

X-ray photoelectron spectroscopy (XPS) was utilized to analyze the surface composition and valence states of Ni@N-HCS-800. The XPS survey spectrum of Ni@N-HCS-800, as shown in Fig. S4a, confirms the presence of Ni, C, N, and O elements on the surface of the catalyst. The high-resolution XPS spectrum of C 1s (Fig. S4b) shows peaks at 284.7, 285.5, and 288.5 eV, corresponding to C–C, C–N, and C–O bonds, respectively.[22] The XPS spectrum of N 1s (Fig. 2c) reveals peaks at 398.7 eV (pyridine N), 399.6 eV (pyrrole N), 401 eV (graphite N), and 403.6 eV (oxidized N), confirming nitrogen doping in the carbon structure.[25,26] With increasing pyrolysis temperature, the relative content of pyridinic N decreased, while that of other N species exhibited a slight increasing trend (Table S1). Specifically, the pyridine-N content declined from 52.3% in Ni@N-HCS-700 to 27.1% in Ni@N-HCS-800, 20.3% in Ni@N-HCS-900, respectively. These could be attributed to residual water molecules in the nitrogen gas, which are preferentially adsorbed onto pyridine-N rather than pyrrolic-N. Consequently, the carbon atoms adjacent to pyridine-N are more susceptible to etching, leading to their relative loss.[27] Prior research has indicated that pyridine-N favors the activity of competitive HER, while pyrrolic N and graphitic N are identified as key sites for CO production.[28–30] Therefore, the Ni@N-HCS-800 catalyst, with its low concentration of pyrrolic-N and nitrogen species balance, demonstrates better catalytic activity. The high-resolution XPS spectrum of Ni 2p revealed similar chemical environments of the Ni element for all samples, as shown in Fig. 2d, characterized by Ni^0 $2p_{3/2}$ (871.8 eV) and $2p_{1/2}$ (854.4 eV) spin–orbit peaks, corresponding to the TEM and XRD results.[31,32] Additionally, a small amount of Ni^{2+} is also detected at 856.3 eV and 873.6 eV, indicating oxidation of the metal. Furthermore, the comparison of elemental content before and after etching revealed a decrease in pyridine-N and oxidized-N species, indicating that pyridine-N is predominantly located on the surface and edges of the carbon matrix,

Open Access Article. Published on 04 February 2026. Downloaded on 4/28/2026 3:51:50 AM.
This article is licensed under a Creative Commons Attribution-NonCommercial 3.0 Unported Licence.

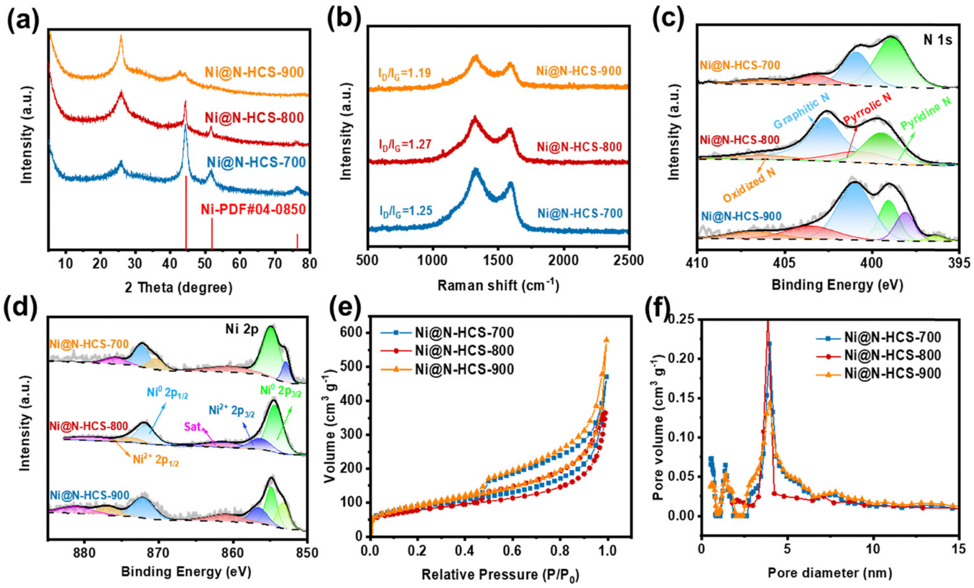

Fig. 2 Characterization of different electrocatalysts. (a) XRD patterns, (b) Raman spectra, (c) high-resolution XPS spectra of N 1s and (d) Ni 2p, (e) N_2 adsorption–desorption isotherms, (f) pore size distributions.

where it is readily dissolved and removed by acid, while oxidized-N is reduced (Table S1). Concurrently, a 1.44% reduction of carbon content suggests the simultaneous removal of unstable and disordered carbon (Table S2). In contrast, the overall surface nitrogen and nickel species content increased, with a notable rise in Ni^{2+} (Fig. S5). This signifies that the etching process alters the electronic structure of the nickel cores, fostering a strong electronic interaction with the N-doped carbon shell.[33] This synergistic structure is beneficial for constituting the highly active sites for the CO_2 reduction reaction.

Electrochemical CO_2 reduction performance

Based on the spectroscopic analysis, the pyrolysis temperature was revealed to substantially modulate the carbon skeleton microstructure, where an optimal content of pyrrolic-N species crucially facilitates CO_2 molecular activation through enhanced electron transfer dynamics. The N_2 adsorption–desorption isotherms in Fig. 2e displayed the type IV hysteresis lines, confirming the existence of the mesoporous structure. The Brunauer–Emmett–Teller (BET) surface area of Ni@N-HCS-700, Ni@N-HCS-800, Ni@N-HCS-900 were 306.258 $m^2\ g^{-1}$, 272.883 $m^2\ g^{-1}$ and 327.704 $m^2\ g^{-1}$, respectively. Additionally, the pore size distribution analysis in Fig. 2f revealed the average pore diameter of 3.9 nm for Ni@N-HCS-700 and Ni@N-HCS-900, while Ni@N-HCS-800 exhibited a distinctly larger pore diameter of 8.2 nm. These findings clearly reveal the predominantly hollow pore structure of Ni@N-HCS-800, facilitating efficient reactant diffusion and electrolyte transport.[34]

To comprehensively evaluate the electrocatalytic performance of Ni@N-HCS towards CO_2RR, a series of systematic tests were conducted. The obtained linear sweep voltammogram (LSV) curves, as illustrated in Fig. 3a, clearly demonstrate that Ni@N-HCS-800 exhibits significantly higher current densities compared to the control samples across all potentials. Analysis of catalytic products using online gas chromatography show that only H_2 and CO gases were detected, indicating the high selectivity of the catalysts towards the CO_2RR (Fig. 3b). Notably, within the potential range of −0.68 to −0.98 V, Ni@N-HCS-800 demonstrates a remarkable faradaic efficiency of CO (FE_{CO}) exceeding 80.0%, with a peak FE_{CO} of 90.38% at −0.78 V. Moreover, Ni@N-HCS-800 demonstrates excellent catalytic activity, with a maximum current density for CO production (j_{CO}) of 18.5 mA cm^{-2} at −0.98 V (Fig. 3c). Importantly, this catalyst exhibits favorable electrocatalytic stability, maintaining a stable current density and FE_{CO} even after 12 h of continuous operation at −0.78 V (Fig. 3d). These results demonstrate the comparable electrocatalytic performance and stability of Ni@N-HCS-800 towards CO_2RR compared to other Ni-based catalysts (Table S3), emphasizing its potential for practical applications in CO_2 conversion technologies.

Additionally, an in-depth investigation was conducted to elucidate the underlying reasons for the intrinsic catalytic activity of the Ni@N-HCS-800 catalyst. The Tafel slope, a key parameter in revealing the reaction kinetics of the electrocatalyst for the CO_2RR, was employed in this study. The lower Tafel slope of 341 mV dec^{-1} for Ni@N-HCS-800, compared to the comparison samples (438 mV dec^{-1} for Ni@N-HCS-700 and 371 mV dec^{-1} for Ni@N-HCS-900), as shown in Fig. 3e, indicates faster reaction kinetics in CO_2RR.[35,36] In general, electrochemical impedance spectroscopy (EIS) was employed to analyze the charge transfer characteristics of the electrocatalysts. Notably, Ni@N-HCS-800 demonstrates a notably lower charge transfer resistance than the control samples, as depicted in Fig. S6, highlighting its superior capability for fast charge transfer.[37] The electrochemically active surface area (ECSA) of the catalysts was determined through the measurement of the electrochemical double-layer capacitance (C_{dl}). Significantly,

© 2026 The Author(s). Published by the Royal Society of Chemistry

Open Access Article. Published on 04 February 2026. Downloaded on 4/28/2026 3:51:50 AM.
This article is licensed under a Creative Commons Attribution-NonCommercial 3.0 Unported Licence.

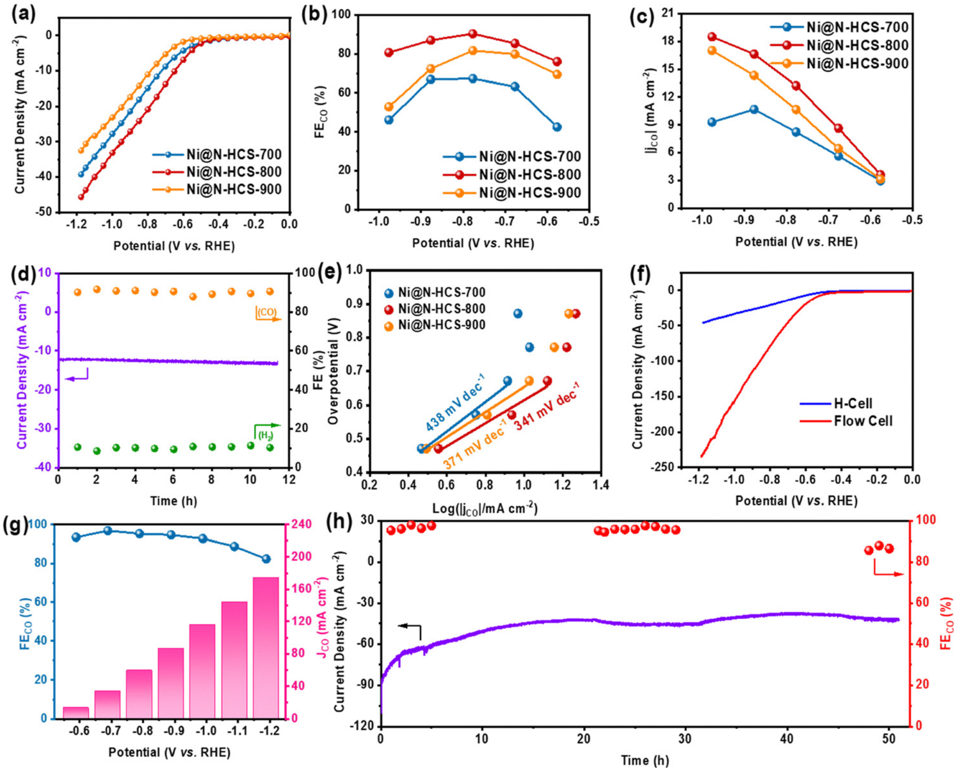

Fig. 3 Electrocatalytic CO_2RR performance. (a) LSV curves, (b) CO faradaic efficiency (FE$_{CO}$), (c) CO partial current density at different potentials and (d) stability test of Ni@N-HCS-800 at −0.78 V *versus* RHE for 10 h in H-cell. (e) Tafel plots of different catalysts in CO_2-saturated 0.5 M $KHCO_3$ electrolytes. (f) LSV curves, (g) FE$_{CO}$ and corresponding current densities, (h) long-term stability test at −0.79 V *vs.* RHE of Ni@N-HCS-800 measured in flow cell.

Ni@N-HCS-800 exhibits a higher C_{dl} value of 70.26 mF cm^{-2}, surpassing that of Ni@N-HCS-700 (67.27 mF cm^{-2}) and Ni@N-HCS-900 (56.11 mF cm^{-2}) (Fig. S7). Additionally, the C_{dl} of Ni@C-800 (42.1 mF cm^{-2}) and Ni@HCS-800 (49.9 mF cm^{-2}) is much lower than that of Ni@N-HCS-800 (Fig. S8). This observation suggests that the hierarchical porous structure of Ni@N-HCS-800 possesses a larger ECSA, enabling the exposure of a greater number of active sites, thereby enhancing its catalytic activity.[38]

It should be noted that the low solubility of CO_2 in aqueous solutions can significantly impede the mass transfer of CO_2 in H-cells, thus limiting their practical applications. To assess the suitability of Ni@N-HCS-800 in industrial applications, performance evaluations using a flow cell with a neutral-alkaline asymmetric electrolyte were performed. The pH difference in the asymmetric electrolyte generates electrochemical neutralization energy, which helps reduce the voltage required for the device.[39] Specifically, a cathodic electrolyte of 3 M KCl solution and an anodic electrolyte of 1 M KOH solution were employed (Fig. S9). Additionally, the existence of the gas diffusion electrodes in the flow cell makes the mass transfer of CO_2 much more efficient, facilitating the CO_2RR. Significantly, as shown in Fig. 3f, the flow cell exhibits excellent performance by achieving an exceptional current density of 235 mA cm^{-2} at −1.19 V, even surpassing the H-cell by nearly 5 times. Fig. 3g shows the faradaic efficiency and current density of Ni@N-HCS-800 as the cathode electrode in the flow cell. The results demonstrate that Ni@N-HCS-800 maintains a remarkable CO selectivity of more than 90% in a wide voltage range from −0.59 to −0.99 V, with the highest FE$_{CO}$ reaching 96.81% at −0.69 V. Notably, j_{CO} reaches an impressive 174.23 mA cm^{-2} at −1.19 V, accompanied by a high FE$_{CO}$ of 82.34%. On the contrary, the FE$_{CO}$ of Ni@C-800 and Ni@HCS-800 are maintained at values below 10% over the whole range of applied potentials, indicating the inferior CO selectivity and substantial competing side reactions (Fig. S10). The comparative results demonstrate that, protected by the DCDA shell, the porous spherical structure offers a distinct advantage with regard to facilitating rapid CO_2 diffusion and electrolyte ion transport.

Furthermore, Ni@N-HCS-800 in the flow cell depicted in Fig. 3h highlights the decent long-term stability. It can operate continuously for over 50 h at −0.79 V, consistently maintaining a stable current density of approximately 50 mA cm^{-2}, while exhibiting a remarkably good selectivity of over 90% for CO production. It is noteworthy that the current density dropped sharply from ∼90 to 50 mA cm^{-2} at the initial reaction stage. This transient behavior can be attributed to the reduction of carbon species, combined with limited electrode wetting and inefficient gas bubble release on the smooth surface. These factors temporarily enhance local current density while hindering mass transfer. In addition, as evidenced by XRD (Fig. S11), the crystalline phase of Ni@N-HCS-800 after a 1 h test reveals the formation of a new nickel carbide phase (NiC_x), which results from the dissolution and subsequent incorporation of

© 2026 The Author(s). Published by the Royal Society of Chemistry

Open Access Article. Published on 04 February 2026. Downloaded on 4/28/2026 3:51:50 AM.
This article is licensed under a Creative Commons Attribution-NonCommercial 3.0 Unported Licence.

carbon-active species into the Ni lattice. The formation of this NiC_x phase is also responsible for the initial current instability. Upon prolonged electrolysis, both the current density and selectivity stabilized, indicating that the newly formed NiC_x phase is ultimately a stable and highly active state. Moreover, this stability was supported by the complete wetting of the electrode surface and the establishment of stable bubble nucleation sites. The SEM image of the catalyst displays that there is little change that occurred in the morphology of Ni@N-HCS-800 after CO_2RR (Fig. S12). XPS of Ni@N-HCS-800 sample reveals chemical valence states of the Ni species remain between Ni^0 and Ni^{2+}. (Fig. S13). The above results clearly confirm that the Ni@N-HCS-800 catalyst retains satisfactory durability after electroreduction.

Performance of Zn–CO_2 battery

Inspired by the excellent CO_2RR activity of Ni@N-HCS-800 catalyst, a homemade Zn–CO_2 flow battery was developed. The battery involved utilizing a carbon paper coated with the Ni@N-HCS-800 catalyst as the cathode and a Zn plate as the anode. The schematic configuration of the Zn–CO_2 flow battery is depicted in Fig. 4a and Fig. S14. A bipolar membrane was implemented to isolate the cathode and anode chambers. For the electrolyte composition, 6 M KOH with 0.2 M $Zn(CH_3COO)_2$ solution was employed as the anolyte, and 1 M $KHCO_3$ solution was used as the catholyte. Additionally, dedicated pumps were employed to facilitate the continuous circulation of the catholyte and anolyte, respectively, ensuring that the performance of the battery does not deteriorate due to changes in electrolyte concentration and pH. During the discharge process of the Zn–CO_2 flow battery, the cathode undergoes CO_2RR while the anode experiences the dissolution of Zn plates, resulting in the formation of $Zn(OH)_4^{2-}$. On the other hand, during the charging process, the cathode facilitates OER while the $Zn(OH)_4^{2-}$ ions are reduced to metallic Zn at the anode.

The effectiveness of Ni@N-HCS-800 as a bifunctional electrocatalyst for both CO_2RR and OER in reversible Zn–CO_2 flow batteries was confirmed through charge–discharge polarization curves, as depicted in Fig. 4b. Additionally, the Zn–CO_2 flow battery utilizing Ni@N-HCS-800 as the cathode exhibits exceptional performance, reaching a maximum power density of 11.55 mW cm^{-2} at a discharge current of 12.03 mA cm^{-2}, outperforming previously reported catalysts (Table S4). The higher power density in the Zn–CO_2 battery can be predominantly governed by three factors: (1) the short distance gap of 2 mm between the working electrode and Zn plate effectively reduces the internal resistance, (2) good electrical conductivity at the anode zinc foil connection, and (3) an optimized flow field design on the gas diffusion electrode side. Meanwhile, this flow battery, employing the Ni@N-HCS-800 cathode, demonstrates stable voltage plateaus at various discharge current densities, accompanied by a high open-circuit voltage of 1.589 V (Fig. 4c).[39] Furthermore, this flow battery demonstrates an impressive FE_{CO} of 87.98% at a current density of 10 mA cm^{-2} (Fig. 4d). These findings highlight the comparable electrochemical performance of the Zn–CO_2 flow battery employing Ni@N-HCS-800 as the cathode material. Therefore, to further obtain the enhanced performance of the Zn–CO_2 battery, it is essential to optimize the electrolyzer configuration. This can be realized through precise adjustments to the composition and concentration of the electrolyte, alongside improved electrical conductivity of the zinc foil electrode. The adoption of a membrane electrode assembly (MEA) also offers a viable pathway for further performance enhancement. Nevertheless, as

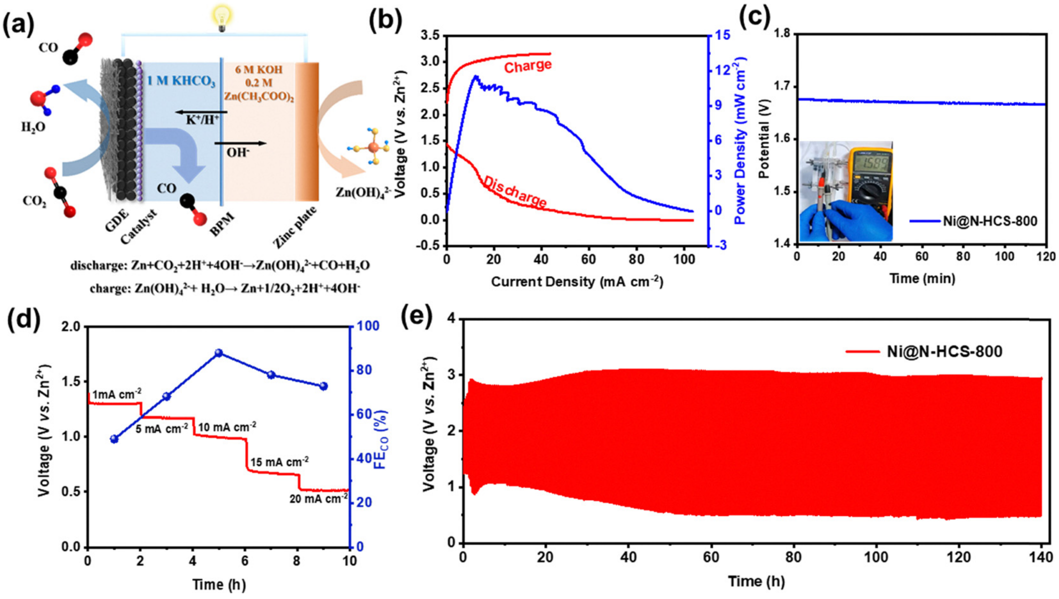

Fig. 4 The aqueous rechargeable Zn–CO_2 electrochemical cell. (a) Schematic setup of the Zn–CO_2 flow battery; (b) polarization curves for discharge and charge, along with corresponding power density; (c) galvanostatic discharge profiles; (d) FE_{CO} values at various current densities; (e) galvanostatic discharge–charge cycling curves at 2 mA cm^{-2} for Ni@N-HCS-800.

© 2026 The Author(s). Published by the Royal Society of Chemistry

Open Access Article. Published on 04 February 2026. Downloaded on 4/28/2026 3:51:50 AM.
This article is licensed under a Creative Commons Attribution-NonCommercial 3.0 Unported Licence.

shown in Fig. 4e, during the charge and discharge processes of the Zn–CO_2 flow battery at a constant current of 2 mA cm^{-2}, an initial decay in performance was observed, which may be attributed to the occurrence of the water flooding phenomenon.[17,40] However, this initial decay stabilizes after 50 h. Remarkably, the Zn–CO_2 flow battery exhibits outstanding cycling durability, with the capability to exceed 400 cycles (equivalent to 140 h) without significant performance degradation. This satisfactory cycling stability further confirms the superior rechargeable durability of the Zn–CO_2 flow battery with Ni@N-HCS-800 as the cathode.

Mechanistic analysis

To verify the reaction pathway of electrochemical CO_2-to-CO reduction, the reaction intermediates generated over the Ni@N-HCS-800 catalyst were monitored by *in situ* Raman spectra during stepwise incremental potential application (Fig. 5a). As shown in Fig. 5b, a new band located at about 279 cm^{-1} could be assigned to the frustrated rotation of adsorbed *CO on the catalyst.[41,42] The strongest *CO signal at −0.78 V indicated the highest *CO coverage at this potential, which facilitates C–C coupling. Progressive decrease in signal intensity with more negative potential is consistent with the decline in CO selectivity. Furthermore, *in situ* electrochemical attenuated total reflectance Fourier transform infrared spectroscopy (ATR-FTIR) of Ni@N-HCS-800 catalyst were employed from −0.28 to −0.98 V in CO_2-saturated 1 M $KHCO_3$ (Fig. 5c and Fig. S15). A characteristic peak at 1913 cm^{-1} emerges at −0.28 V, corresponding to the C≡O stretch of linearly adsorbed CO, implying the formation of *CO intermediate.[43,44] The intensity of this peak maximizes at −0.78 V before declining at more negative potentials, indicating that the active sites were not poisoned.

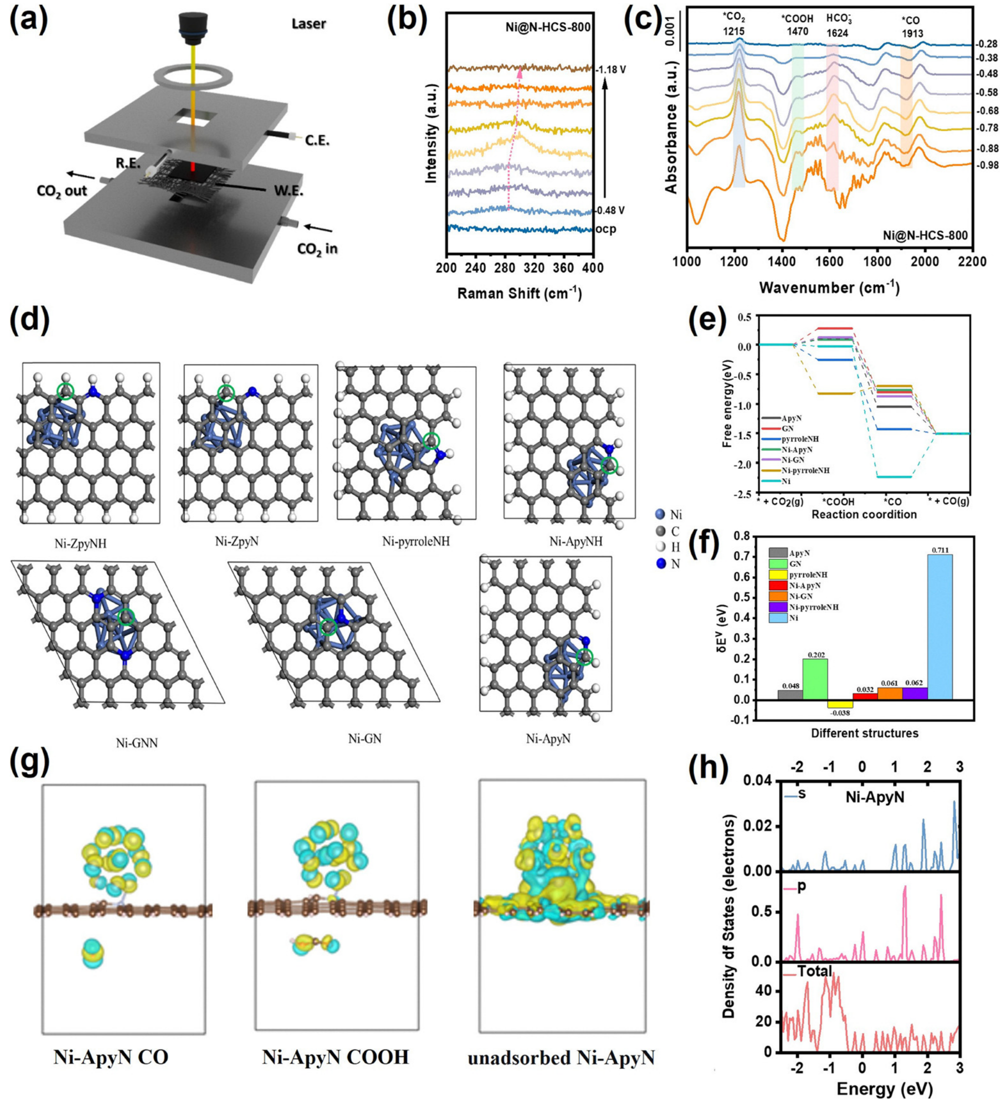

Fig. 5 (a) Scheme of *in situ* Raman spectroscopy during CO_2RR electrocatalysis. (b) *In situ* Raman spectroscopy of Ni@N-HCS-800 catalysts in CO_2-saturated 1 M $KHCO_3$. (c) *In situ* spectra recorded at different potentials for Ni@N-HCS-800 catalysts. (d) Graphene-covered Ni clusters. The free energy diagrams (FED) of CO_2RR (e) on the optimal active site for each type and the δE^V values of CO_2RR (f) on the optimal active site for each type. (g) The Charge density maps of Ni-ApyN. (h) Projected Density of States (PDOS) analysis of Ni-ApyN.

Open Access Article. Published on 04 February 2026. Downloaded on 4/28/2026 3:51:50 AM.
This article is licensed under a Creative Commons Attribution-NonCommercial 3.0 Unported Licence.

Specifically, the peaks at 1215 cm^{-1} on the surface could be assigned to $*CO_2^-$ intermediates, which were gradually strengthened with increasing applied potentials, suggesting the adsorbed CO_2 was activated.[45] Besides, the band at 1470 cm^{-1} was attributed to the vibration of O–C–O in the two-oxygen bridge *COOH, while the bidentate carbonate group was observed at 1624 cm^{-1}.[46,47] These results demonstrated that the enhanced performance of CO production was improved by facilitating the adsorption of *COOH during the electrochemical CO_2RR.

The utilization of density functional theory (DFT) offers crucial insights into the outstanding performance of the Ni@N-HCS-800 catalyst in CO_2RR. All possible active sites present on Ni@N-HCS-800 catalysts were calculated, including armchair edge sites of pyridinic N at the edge with and without hydrogeneration (ApyN and ApyNH), the zigzag edge sites with and without hydrogeneration (ZpyN and ZpyNH), pyrrole edge (pyrroleNH), N-doped graphene (GN) and dual N-doped graphene (GNN), as illustrated in Fig. S16. These specific sites have been identified as being exposed and pertinent to the CO_2RR in previous research studies.[48,49] Additionally, the structure of graphene-covered metal based on experimental TEM images was constructed (Fig. 1e), comprising graphene-covered Ni clusters (Ni-ApyN, Ni-ApyNH, Ni-ZpyN, Ni-ZpyNH, Ni-pyrroleNH, Ni-GN, Ni-GNN, depicted as in Fig. 5d). The energy pathway of the reaction was assessed using the computational hydrogen electrode (CHE) method,[49] with the virtual energetic span (δE_v) serving as the activity-determining parameter.[50] Detailed information can be found in the SI. CO_2RR calculations were conducted for all possible active sites on graphene-covered metals (Fig. S17). The outcomes reveal that the most efficient active sites for CO_2RR are Ni-ApyN, pyrroleNH, ApyN, and Ni-GN, as illustrated in Fig. 5e. When assessed through δEv, it becomes evident that the Ni-ApyN structure exhibits the highest catalytic activity in CO_2RR, with an energy of only 0.032 eV, as shown in Fig. 5f. These findings strongly emphasize the exceptional suitability of pyridine N-doped carbon-coated Ni nanoparticles within the Ni@N-HCS-800 catalyst for the CO_2RR process.

The differential charge density analysis visually elucidates the electronic modulation effect induced by the pyridinic N species (Fig. 5g and Fig. S18). In contrast to Ni-GN, the Ni-ApyN structure exhibits more pronounced electron accumulation (yellow regions) and depletion (cyan regions) at the metal–support interface, verifying the induction of a robust metal–support interaction.[51] Crucially, during the adsorption of CO and COOH intermediates, Ni-ApyN facilitates a potent directional electron transfer from the Ni active sites to the antibonding orbitals of the intermediates. Furthermore, the projected density of states (PDOS) analysis reveals the pivotal role of the support in regulating the local electronic environment (Fig. 5h and Fig. S19). Unlike the diffuse electronic state distribution observed in Ni-GN, Ni-ApyN displays significantly enhanced and sharp C(2p) density of states peaks within the valence band (specifically from -1.5 eV to -0.5 eV). These high-intensity localized electronic states exhibit a high degree of overlap with the Ni 3d orbital energy levels, confirming the existence of stronger C(2p)–Ni(3d) orbital resonance hybridization in the ApyN system.[52] Consequently, the d-band center of Ni-ApyN is positively shifted to -3.28 eV (compared to -3.32 eV for Ni-GN). According to the d-band center theory,[53] this upshift mitigates the electron filling of metal-adsorbate antibonding orbitals during the adsorption process, thereby effectively strengthening the binding affinity between the active sites and key intermediates, which is favorable for accelerating the reaction kinetics.

Conclusions

In summary, Ni@N-HCS-800 catalysts composed of surface porous N-doped hollow urchin-like carbon spheres encapsulated with nickel nanoparticles have been successfully synthesized using Ni-MOF precursors, which exhibit remarkable electrochemical CO_2 reduction performance. The utilization of the homemade flow cell demonstrates its capability to achieve an industrial-grade current density of 174.23 mA cm^{-2}, accompanied by a high FE_{CO} of 82.34%, while operating continuously for 50 h at a current density of 50 mA cm^{-2}. Notably, the Zn–CO_2 flow battery incorporating Ni@N-HCS-800 as the cathode exhibits the highest power density of 11.55 mW cm^{-2} and exceptional charge–discharge cycle stability for 140 h. Density functional theory (DFT) calculations have conclusively established that the Ni-ApyN structure serves as the optimized active site within the catalyst, and the pyridine N-doped carbon layer coated with Ni NPs had a significant effect on enhancing the catalytic activity of the catalysts and lowering the energy barrier for the reaction. These findings highlight the significance of rational design of catalyst structures to enhance the electrocatalytic activity. Furthermore, the outstanding performance of Ni@N-HCS-800 in both the flow cell and Zn–CO_2 flow battery provides valuable insights to advance research on energy storage and conversion.

Author contributions

Songjiang Wu, Di Wang: conceptualization, data curation, writing – original draft. Haijian Wang: software. Haiyan Chen, Shenjie Yu: investigation, methodology. Xinyu Zhuang: software. Hao Zhang: writing – review & editing. Suqin Ci, Zhenhai Wen: funding acquisition, supervision, project administration.

Conflicts of interest

The authors declare that they have no known competing financial interests or personal relationships that could have appeared to influence the work reported in this paper.

Data availability

The data supporting this article have been included as part of the supplementary information (SI). Supplementary information is available. See DOI: https://doi.org/10.1039/d5ey00299k.

© 2026 The Author(s). Published by the Royal Society of Chemistry

Open Access Article. Published on 04 February 2026. Downloaded on 4/28/2026 3:51:50 AM.
This article is licensed under a Creative Commons Attribution-NonCommercial 3.0 Unported Licence.

Acknowledgements

This work was financially supported by the National Natural Science Foundation of China (22168025).

References

1 F. Wang, G. Wang, P. Deng, Y. Chen, J. Li, D. Wu, Z. Wang, C. Wang, Y. Hua and X. Tian, *Small*, 2023, **19**, 2301128.

2 C. Yan, H. Li, Y. Ye, H. Wu, F. Cai, R. Si, J. Xiao, S. Miao, S. Xie, F. Yang, Y. Li, G. Wang and X. Bao, *Energy Environ. Sci.*, 2018, **11**, 1204–1210.

3 W. Ren, X. Tan, W. Yang, C. Jia, S. Xu, K. Wang, S. C. Smith and C. Zhao, *Angew. Chem., Int. Ed.*, 2019, **58**, 6972–6976.

4 L. Zhang, J. Feng, S. Liu, X. Tan, L. Wu, S. Jia, L. Xu, X. Ma, X. Song, J. Ma, X. Sun and B. Han, *Adv. Mater.*, 2023, **35**, 2209590.

5 C. He, S. Chen, R. Long, L. Song and Y. Xiong, *Sci. China: Chem.*, 2020, **63**, 1721–1726.

6 R.-X. Yang, Y.-R. Wang, G.-K. Gao, L. Chen, Y. Chen, S.-L. Li and Y.-Q. Lan, *Small Struct.*, 2021, **2**, 2100012.

7 J.-H. Liu, X. Cao, R. Wang, X. Chen, Y. Wang, P. Yang, J. Long, X. Yin, Z. Huang and D. Cao, *Sci. China Mater.*, 2023, **66**, 2741–2749.

8 P. Yao, J. Zhang, Y. Qiu, Q. Zheng, H. Zhang, J. Yan and X. Li, *ACS Sustainable Chem. Eng.*, 2021, **9**, 5437–5444.

9 C.-Z. Yuan, L.-Y. Zhan, S.-J. Liu, F. Chen, H. Lin, X.-L. Wu and J. Chen, *Inorg. Chem. Front.*, 2020, **7**, 1719–1725.

10 Z. Cao, P. Su, X. Wang, X. Liu, Y. Ma, C. Li, S. Ping Jiang and J. Liu, *Fuel*, 2022, **321**, 124043.

11 Y. Li, S. L. Zhang, W. Cheng, Y. Chen, D. Luan, S. Gao and X. W. Lou, *Adv. Mater.*, 2021, **34**, 2105204.

12 Q.-L. Zhu, W. Xia, T. Akita, R. Zou and Q. Xu, *Adv. Mater.*, 2016, **28**, 6391–6398.

13 Y. Li, X. F. Lu, S. Xi, D. Luan, X. Wang and X.-W. Lou, *Angew. Chem., Int. Ed.*, 2022, **61**, e202201491.

14 H. Wang, X. Wu, G. Liu, S. Wu and R. Xu, *Nano Res.*, 2022, **16**, 4546–4553.

15 Y. Niu, C. Zhang, Y. Wang, D. Fang, L. Zhang and C. Wang, *ChemSusChem*, 2012, **14**, 1140–1154.

16 Y. Kim, E. W. Lees and C. P. Berlinguette, *ACS Energy Lett.*, 2022, **7**, 2382–2387.

17 A. Inoue, T. Harada, S. Nakanishi and K. Kamiya, *EES Catal.*, 2023, **1**, 9–16.

18 T. Wang, X. Sang, W. Zheng, B. Yang, S. Yao, C. Lei, Z. Li, Q. He, J. Lu, L. Lei, L. Dai and Y. Hou, *Adv. Mater.*, 2020, **32**, 2002430.

19 M. Yang, S. Liu, J. Sun, M. Jin, R. Fu, S. Zhang, H. Li, Z. Sun, J. Luo and X. Liu, *Appl. Catal., B*, 2022, **307**, 121145.

20 S. Gong, W. Wang, C. Zhang, M. Zhu, R. Lu, J. Ye, H. Yang, C. Wu, J. Liu, D. Rao, S. Shao and X. Lv, *Adv. Funct. Mater.*, 2022, **32**, 2110649.

21 A. Kundu, A. Samanta and C. R. Raj, *ACS Appl. Mater. Interfaces*, 2021, **13**, 30486–30496.

22 L. Yan, Y. Xu, P. Chen, S. Zhang, H. Jiang, L. Yang, Y. Wang, L. Zhang, J. Shen, X. Zhao and L. Wang, *Adv. Mater.*, 2020, **32**, 2003313.

23 M. Wang, Q. Xie, H. Chen, G. Liu, X. Cui and L. Jiang, *Chin. J. Catal.*, 2021, **42**, 2306–2312.

24 Z. Qiao, S. Hwang, X. Li, C. Wang, W. Samarakoon, S. Karakalos, D. Li, M. Chen, Y. He, M. Wang, Z. Liu, G. Wang, H. Zhou, Z. Feng, D. Su, J. S. Spendelow and G. Wu, *Energy Environ. Sci.*, 2019, **12**, 2830–2841.

25 X. Han, T. Zhang, X. Wang, Z. Zhang, Y. Li, Y. Qin, B. Wang, A. Han and J. Liu, *Nat. Commun.*, 2022, **13**, 2900.

26 K. Chen, Z. Wen, P. Cai, G. Wang, S. Ci and K. Li, *Appl. Catal., B*, 2021, **295**, 120275.

27 L. Han, C. Wang, H. Xu, M. Yang, B. Li and M. Liu, *J. Mater. Chem. A*, 2025, **13**, 2707–2715.

28 Q. He, Y. Zhang, H. Li, Y. Yang, S. Chen, W. Yan, J. Dong, X.-M. Zhang and X. Fan, *Small*, 2022, **18**, 2108034.

29 W. Xiong, H. Li, H. Wang, J. Yi, H. You, S. Zhang, Y. Hou, M. Cao, T. Zhang and R. Cao, *Small*, 2020, **16**, 2003943.

30 X. Cui, Z. Pan, L. Zhang, H. Peng and G. Zheng, *Adv. Energy Mater.*, 2017, **7**, 1701456.

31 Q. Lu, C. Chen, Q. Di, W. Liu, X. Sun, Y. Tuo, Y. Zhou, Y. Pan, X. Feng, L. Li, D. Chen and J. Zhang, *ACS Catal.*, 2022, **12**, 1364–1374.

32 Z. Yu, X. Lv, J. Chen, Y. Lv, X. Liu, S. Yang and Y. Liu, *ChemistrySelect*, 2022, **7**, e202202055.

33 S. Yi, X. Qin, C. Liang, J. Li, R. Rajagopalan, Z. Zhang, J. Song, Y. Tang, F. Cheng, H. Wang and M. Shao, *Appl. Catal., B*, 2020, **264**, 118537.

34 T. Yang, W. Xie, N. Tian, X.-H. Liu and X. Zhang, *J. Alloys Compd.*, 2022, **904**, 164042.

35 R. He, A. Zhang, Y. Ding, T. Kong, Q. Xiao, H. Li, Y. Liu and J. Zeng, *Adv. Mater.*, 2018, **30**, 1705872.

36 C. Hu, S. Bai, L. Gao, S. Liang, J. Yang, S.-D. Cheng, S.-B. Mi and J. Qiu, *ACS Catal.*, 2019, **9**, 11579–11588.

37 G. Wang, J. Chen, K. Li, J. Huang, Y. Huang, Y. Liu, X. Hu, B. Zhao, L. Yi, T. W. Jones and Z. Wen, *Nano Energy*, 2022, **92**, 106751.

38 C. Chen, X. Sun, X. Yan, Y. Wu, H. Liu, Q. Zhu, B. B. A. Bediako and B. Han, *Angew. Chem., Int. Ed.*, 2020, **59**, 11123–11129.

39 Y. Ding, P. Cai and Z. Wen, *Chem. Soc. Rev.*, 2021, **50**, 1495–1511.

40 L. Li, J. Chen, V. S. S. Mosali, Y. Liang, A. M. Bond, Q. Gu and J. Zhang, *Angew. Chem., Int. Ed.*, 2022, **61**, e202208534.

41 L. Zhang, J. Feng, L. Wu, X. Ma, X. Song, S. Jia, X. Tan, X. Jin, Q. Zhu, X. Kang, J. Ma, Q. Qian, L. Zheng, X. Sun and B. Han, *J. Am. Chem. Soc.*, 2023, **145**, 21945–21954.

42 L. Xiong, X. Zhang, H. Yuan, Y. Lian, H. Jin, H. Sun, Z. Deng, D. Wang, J. Hu, J. Choi, J. Li, Y. Chen, J. Zhong, J. Guo, M. H. Rümmerli, L. Xu and Y. Peng, *Angew. Chem., Int. Ed.*, 2020, **60**, 2508–2518.

43 C. Cao, S. Zhou, S. Zou, H. Zhang, B. Chen, J. Huang, X.-T. Wu, Q. Xu and Q.-L. Zhu, *Research*, 2023, **6**, 0079.

44 Y. Sheng, Y. Guo, H. Yu, K. Deng, Z. Wang, X. Li, H. Wang, L. Wang and Y. Xu, *Small*, 2023, **19**, 2207305.

© 2026 The Author(s). Published by the Royal Society of Chemistry

Open Access Article. Published on 04 February 2026. Downloaded on 4/28/2026 3:51:50 AM.
This article is licensed under a Creative Commons Attribution-NonCommercial 3.0 Unported Licence.

45 Z. Jiang, M. Zhang, X. Chen, B. Wang, W. Fan, C. Yang, Z. Zhang, X. Yang, C. Li and T. Zhou, *Angew. Chem., Int. Ed.*, 2023, **62**, 202311223.

46 M. Wang, S. Liu, B. Chen, F. Tian and C. Peng, *ACS Sustainable Chem. Eng.*, 2022, **10**, 5693–5701.

47 S. Wu, H. Chen, C. Jia, L. Liao, K. Chen, S. Ci, Q. Xu and Z. Wen, *Inorg. Chem. Front.*, 2023, **10**, 4484–4495.

48 Y. Wang, J. Chen, G. Wang, Y. Li and Z. Wen, *Angew. Chem., Int. Ed.*, 2018, **57**, 13120–13124.

49 J. K. Nørskov, J. Rossmeisl, A. Logadottir, L. Lindqvist, J. R. Kitchin, T. Bligaard and H. Jónsson, *J. Phys. Chem. B*, 2004, **108**, 17886–17892.

50 J. Chen, Y. Chen, P. Li, Z. Wen and S. Chen, *ACS Catal.*, 2018, **8**, 10590–10598.

51 C. T. Campbell, *Nat. Chem.*, 2012, **4**, 597–598.

52 R. Hoffmann, *Rev. Mod. Phys.*, 1988, **60**, 601.

53 B. Hammer and J. L. Nørskov, *Surf. Sci.*, 1995, **343**, 211–220.

© 2026 The Author(s). Published by the Royal Society of Chemistry